JOURNAL OF SPACECRAFT AND ROCKETS
Vol. 36, No. 6, November–December 1999

Effects of Welding-Induced Imperfections on Behavior of Space Shuttle Superlightweight Tank

Michael P. Nemeth,* Richard D. Young,† Timothy J. Collins,‡ and James H. Starnes Jr.§
NASA Langley Research Center, Hampton, Virginia 23681-2199

Results of linear-bifurcation buckling and nonlinear analyses of the Space Shuttle superlightweight external liquid-oxygen tank are presented for an important prelaunch loading condition. These results show the effects of actual, measured welding-induced initial geometric imperfections on an important response mode for thin-walled shells that are subjected to combined mechanical and thermal loads. This type of initial geometric imperfection may be encountered in the design of other liquid-fuel launch vehicles. Results are presented that show that the liquid-oxygen tank will buckle in the barrel section, but at load levels nearly four times the magnitude of the operational load level, and will exhibit stable postbuckling behavior. The actual measured imperfections are located in this section of the tank. Results of imperfection sensitivity analyses are presented that show that the largest degradation in the apparent membrane stiffnesses of the liquid-oxygen tank barrel section is caused by an imperfection shape that is in the form of the linear-bifurcation buckling mode with a relatively small amplitude. These results also show that the effect of the relatively large-amplitude measured imperfection is benign.

Introduction

CONSTRUCTION of the International Space Station (ISS) has created a requirement for the Space Shuttle to deliver a large number of payloads to a 51.6-deg high-inclination orbit. Until recently, achieving this orbit required the payload capacity of the orbiter be reduced by approximately 10,000 lb. To recover most of this lost payload capacity, and to minimize the number of Space Shuttle flights needed to build the ISS, NASA developed a new, lighter-weight external fuel tank for the Space Shuttle. This new design, referred to as the superlightweight (SLWT) external tank, is made primarily of an aluminum–lithium alloy and weighs approximately 58,000 lb, which is approximately 8000 lb lighter than the lightweight aluminum external tank previously in service. This 8000-lb weight savings translates into an 8000-lb increase in the payload capacity for the orbiter. The new SLWT tank flew for the first time on 2 June 1998 (Space Transportation System-mission 91).

Important considerations in the design of the SLWT tank are the nonlinear behavior of its thin walled regions that experience compressive and shear stresses and the sensitivity of the response to initial geometric imperfections. Small initial geometric imperfections are known to cause premature, and sometimes unexpected, buckling of thin shell structures. These effects are very important for the SLWT tank because local or global buckling of the shell wall could cause the thermal protection system (TPS) to separate from the tank, which could cause the vehicle to fail. As part of a plan to ensure that the design does not have a shell-wall instability, accurate predictions of the nonlinear response and imperfection sensitivity of the SLWT tank are needed. Accurate predictions of the nonlinear response of the SLWT tank have been shown to require a large-scale, high-fidelity, finite element model to represent the complex structural details of the SLWT tank, and a robust nonlinear shell analysis capability that can predict local and general instability buckling modes.[1,2]

One component of the SLWT tank that experiences significant compressive stresses is the liquid-oxygen (LO_2) tank. The weights of the liquid-hydrogen (LH_2) tank, the LO_2 tank, and the fuel are reacted at the solid-rocket-booster (SRB) attachment points, which causes meridional compressive stresses and shear stresses that extend into the nose of the SLWT tank. After welding the first SLWT LO_2 tank flight article, relatively large initial geometric imperfections were found and measured, and the effects of these large imperfections became a major concern in the development of the tank (N. Otte, Space Shuttle Superlightweight External Tank Project Engineer, NASA Marshall Space Flight Center, private communication, 1996).

The present paper presents results of linear-bifurcation buckling and nonlinear analyses of the SLWT LO_2 tank that were conducted at the NASA Langley Research Center to determine the effects of these large welding-induced initial geometric imperfections on the shell response. These results are for a critical prelaunch loading condition that causes high compressive and shear stresses in the barrel section of the LO_2 tank, where the initial imperfections are pronounced. The objective of the present paper is to identify and articulate the effects of these imperfections on the nonlinear shell response. To fulfill this objective, an overview of the SLWT tank structure and the details of the loading condition are presented first. Then, details of the finite element modeling and load simulation are summarized. Next, details of the initial geometric imperfection measurements and finite element analysis results are presented. These results illustrate the differences in the sensitivity of the nonlinear shell response to the measured welding-induced initial geometric imperfections and to imperfections in the form of the linear-bifurcation buckling mode. Throughout the paper, generic aspects of the finite element models, analyses, and results appear that should be of interest to designers of liquid-fuel launch vehicles.

Overview of the Structure

The Space Shuttle consists of the orbiter, two SRBs, and the external tank (ET), as shown in Fig. 1. The ET consists of a LO_2 tank, a LH_2 tank, and an intermediate structure called the intertank (Fig. 1). The intertank transmits the weight of the fuel, the ET structural weight, and the orbiter weight to the SRBs prior to launch and transmits thrust loads from the SRBs and the orbiter to the ET during ascent. The SLWT LO_2 tank is a thin-walled monocoque shell made primarily of 2195 aluminum–lithium alloy. The LO_2 tank is approximately 49 ft long and has a maximum diameter of approximately 27.5 ft, as indicated in Fig. 2. The LO_2 tank consists of a forward-ogive section made from 8 gore panels, an aft-ogive section made from 12 gore panels, a cylindrical barrel section made from

Received 27 April 1998; revision received 17 April 1999; accepted for publication 2 July 1999.

*Senior Research Engineer, Structural Mechanics Branch, Structures Division. Associate Fellow AIAA.
†Aerospace Engineer, Structural Mechanics Branch, Structures Division. Member AIAA.
‡Aerospace Engineer, Structural Mechanics Branch, Structures Division.
§Head, Structural Mechanics Branch, Structures Division. Fellow AIAA.

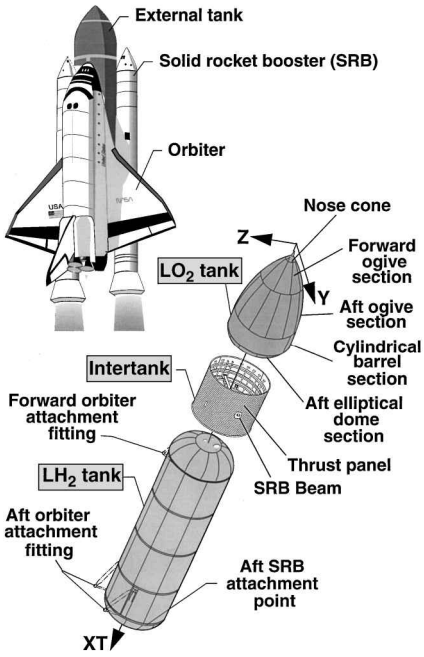

Fig. 1 Space Shuttle external tank components.

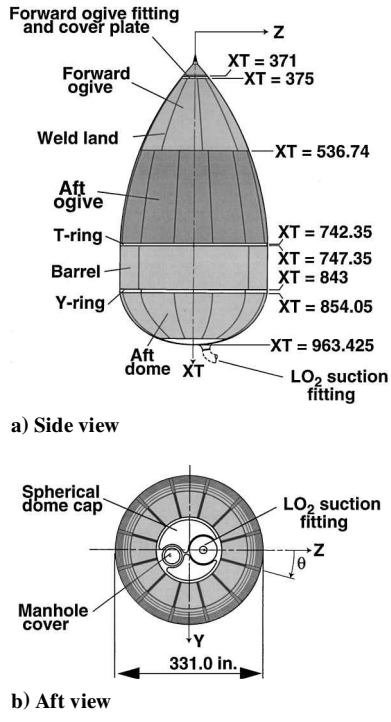

Fig. 2 Space Shuttle external LO_2 tank components; values of XT are given in inches.

4 barrel panels, and an aft elliptical dome section made from 12 gore panels. The coordinate systems used to locate the elements of the LO_2 tank and the intertank also are shown in Figs. 1 and 2. The coordinates (XT, Y, Z) are typically referred to as the global coordinate system of the ET, and axial positions along the tank are indicated by the coordinate value of XT in inches. For example, the location of the junction between the forward and aft ogives is indicated by writing $XT = 536.74$ in. Cylindrical coordinates are also used and are given by (XT, r, θ), where a positive value of θ is measured from the positive Z axis toward the positive Y axis, as shown in Fig. 2b.

The LO_2 tank also has a forward ring frame with a T-shaped cross section that is referred to herein as the T-ring frame, and an aft ring frame with a Y-shaped cross section that is referred to herein as the Y-ring frame. These two ring frames support a baffle assembly that prevents the fuel from sloshing during ascent. The slosh baffle, a lightweight (approximately 455 lb), thin-walled structure, is supported by deep, thin-walled rings at each end that attach to the forward T-ring and the aft Y-ring frames. Other parts of the LO_2 tank include a nonstructural nose cone, a forged forward-ogive fitting and cover plate, an aft spherical dome cap that contains the LO_2 suction fitting and a covered manhole, and a vortex baffle attached to the base of the aft dome cap. The LO_2 tank gore and barrel panels are stretch formed, chemically milled, and then welded together. The panels are fabricated with substantial thickness tailoring to reduce structural weight. The panels are somewhat thicker at the welds to form a stiffenerlike region that is used as a weld land. The primary role of the weld lands is to compensate for any reduction in shell-wall strength that is caused by welding. Tapering the weld lands in thickness and width along their length reduces weight and alleviates stress concentrations in the shell that result from abrupt changes in thickness.

The intertank is a right-circular cylinder that is made from 2090 aluminum–lithium and 7075 aluminum alloys and is shown in Fig. 1. The approximately 22.5-ft-long intertank has a diameter of approximately 27.5 ft and consists of six 45-deg curved panels that are stiffened longitudinally with external hat stiffeners and that are referred to herein as skin-stringer panels. The intertank also has two massive, 45-deg curved panels, referred to as thrust panels, located perpendicular to the Y axis of the intertank (see Fig. 1), and these panels are stiffened longitudinally with integrally machined external blade stiffeners. These eight panels are assembled into the intertank with mechanical fasteners and are attached to five large internal ring frames, a forward flange, and an aft flange. Longitudinal straps (referred to herein as roll ties) suppress lateral-torsional deflection of the ring frames. The main central ring frame, two thrust panel longerons, and the thrust panels are connected to each end of a tapered beam that is referred to herein as the SRB beam (see Fig. 1). The SRB beam spans the diameter of the intertank along the Y axis and has a maximum depth (in the XT direction) of approximately 43 in. at its midspan. Forged fittings (referred to herein as SRB thrust fittings) that are incapable of transmitting moments are fastened to the ends of the SRB beam. The primary role of the thrust panels is to diffuse the large axial loads introduced by the SRBs into the intertank and then into the LO_2 tank shell wall. The SRB beam compensates for the eccentricity of the concentrated loads introduced by the SRBs. The SRB beam also supports the loads normal to the intertank (parallel to the SRB beam) at the SRB attachment points. The intertank also has a 46-in.-high by 52-in.-wide frame-reinforced nonstructural access door located along the cylinder generator at approximately $\theta = 146$ deg.

Critical Loading Condition

The critical SLWT tank loading condition that was used to assess the importance of the welding-induced initial geometric imperfections was identified and supplied by the members of the SLWT tank structural verification team at the NASA Marshall Space Flight Center and the Lockheed Martin Michoud Space Systems Division. This critical loading condition corresponds to prelaunch fueling conditions in which the LH_2 tank is filled with propellant and the LO_2 tank is empty. This loading condition has been described in detail in Refs. 1 and 2. In addition, this loading condition was identified as a worst-case condition, and, as a result, no attempts are made in the present study to address issues of loading imperfections or perturbations, with the exception of the wind loading. Details of this prelaunch loading condition are shown in Fig. 3 and discussed subsequently for convenience.

The loads consist of a wind load, the structural weight, the SRB interface forces, and the LH_2 tank interface force and moment. In addition, there is no ullage pressure and no temperature change in the LO_2 tank. However, the lower 45 in. of the intertank are subjected to an axisymmetric, uniform through-the-thickness temperature field that varies linearly from -423°F, where the intertank is attached to the LH_2 tank ($XT = 1129$ in.), to 50°F at the top of the LH_2 tank forward dome ($XT = 1084$ in.). The nominal ambient temperature of the LO_2 tank and the intertank prior to fueling is 50°F. The SRB interface forces are given by $\boldsymbol{R}_1 = -224.092\boldsymbol{i} - 52.223\boldsymbol{j} - 28.954\boldsymbol{k}$ kips (1 kip = 1000 lb)

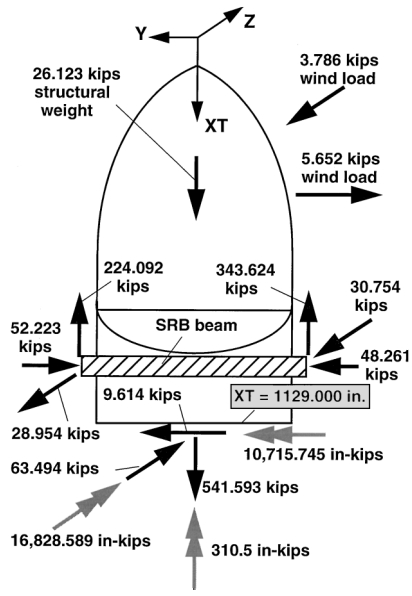

Fig. 3 Prelaunch loads.

and $\boldsymbol{R}_2 = -343.624\boldsymbol{i} + 48.261\boldsymbol{j} - 30.754\boldsymbol{k}$ kips, where the vectors $\boldsymbol{R}_1$ and $\boldsymbol{R}_2$ correspond to the $+Y$ and $-Y$ ends of the SRB beam that is shown in Fig. 3. The vectors $\boldsymbol{i}$, $\boldsymbol{j}$, and $\boldsymbol{k}$ are standard orthonormal base vectors associated with the XT, Y, and Z axes, respectively. Similarly, the interface force and moment between the intertank and the LH_2 tank at $XT = 1129$ in. are given by $\boldsymbol{F} = 541.593\boldsymbol{i} + 9.614\boldsymbol{j} + 63.494\boldsymbol{k}$ kips and $\boldsymbol{M} = -310.500\boldsymbol{i} + 10{,}715.745\boldsymbol{j} + 16{,}828.589\boldsymbol{k}$ in.-kips. The wind pressure that acts on the LO_2 tank and the intertank has a resultant force given by $-5.652\boldsymbol{j} - 3.786\boldsymbol{k}$ kips. Comparison of the magnitude of the wind load with the other loads that act on the structure indicates that the wind load is relatively small. The actual wind pressure distribution that was input into the finite element models is somewhat complicated and, as a result, is not presented herein.

Analysis Code and Finite Element Modeling

The results of the elastic, linear-bifurcation buckling and nonlinear analyses were obtained with the STAGS nonlinear structural analysis code for general shells.[3] The finite element models of the SLWT tank that were used in the present study are very complex and include many structural details and the skin thickness variations or tailoring used to reduce structural weight; for example, see Ref. 4. A detailed description of these models is presented in Ref. 1. STAGS was chosen for analyzing the SLWT tank because of its robust state-of-the-art nonlinear-equation solution algorithms and its general user-input capability that is convenient for modeling branched shells that are typically used for launch vehicles. The shell elements that were used to model the SLWT tank response are based on classical thin-shell theory. The use of these elements is justifed because the ratio of the wall thickness to the minimum radius of curvature at each point of the undeformed LO_2 tank is typically much less than 0.1 and, as will be shown, because the ratio of the largest thickness of the shell wall that forms a given deformation pattern to the smallest characteristic length of the deformation pattern is less than 0.1 (see Ref. 2). A description of the attributes of STAGS and how the features of STAGS were used in the present study to model the SLWT LO_2 tank and intertank are presented in Refs. 3 and 4. The finite element modeling details for the SLWT LO_2 tank and intertank are lengthy and are not presented herein; they are discussed in Refs. 1, 2, and 4.

The basic approach used in the present study to simulate the actual prelaunch loading process is to apply all of the loads illustrated in Fig. 3 to the model, except for the SRB interface loads. This approach is described in detail in Ref. 1. The nodes on the ends of the SRB beam, where the SRB forces act (see Fig. 3), were restrained so that the SRB interface forces become reactions and rigid-body motion is eliminated. Next, the applied loads were separated into two groups. The first group of loads contains the LH_2 tank interface force and moment that are treated as the primary source of destabilizing compressive stresses in the LO_2 tank. This group of loads was identified by the SLWT tank structural verification team as the primary source of destabilizing compressive stresses in the LO_2 tank that may occur at load levels greater than the corresponding operational load level. The second group of loads consists of the wind load, the structural weight, and the weight of the slosh baffle that is located inside the barrel section of the LO_2 tank. The loads in the second group are constant in value, are part of the operational loads, and are considered to be passive loads when determining the stability margin of safety of the LO_2 tank. In performing linear-bifurcation buckling and nonlinear analyses with STAGS, two load factors, p_a and p_b, were assigned to the first (active) and second (passive) load groups, respectively.

As discussed in Ref. 2, analyses were conducted with and without the relatively small wind loads. Neglecting the wind loads was found to have an essentially negligible effect on the results. The results that are presented in the present paper are for no wind loads.

Imperfection Measurement and Shape

During construction of the first SLWT tank flight article, relatively large initial geometric imperfections were found in the LO_2 tank barrel section, next to the meridional weld lands, after the barrel section was welded together into a cylinder. Because of the uncertainty of their importance on the stability of the shell, initial geometric-imperfection measurements were made on the barrel by staff members of the Lockheed Martin Michoud Space Systems Division (Otte, private communication cited earlier). The measurements were made by placing one end of the barrel on several evenly spaced pedestals and then surveying the barrel with a laser tracking system. The entire barrel was not measured. Only four sections of the barrel that surround each of the four weld lands were measured. These sections span an axial length of 95.651 in. and the circumferential locations are given by $21.462 \le \theta \le 73.385$ deg, $107.308 \le \theta \le 158.538$ deg, $202.154 \le \theta \le 253.384$ deg, and $287.308 \le \theta \le 339.232$ deg. For each section of the barrel, a laser target was moved over a rectangular grid that had 49 points along the barrel length, 75 or 76 points along the barrel circumference, and a 2×2-in. mesh spacing. After measuring one section of the barrel, the laser setup was moved to another convenient location to measure the next section. After completion of the barrel measurements, midsurface inital imperfection data were calculated to account for the highly variable thickness distribution of the barrel.

Synthesis of the measured initial geometric imperfection data was done to obtain an imperfection shape for use in a nonlinear stability analysis of the LO_2 tank. The synthesis was done by staff members of the Lockheed Martin Engineering Sciences and Services Company (W. A. Waters Jr., private communication, 1997) by using the measured initial geometric imperfection data reduction capability of DISDECO.[5,6] This data reduction capability of DISDECO is a modern version of the procedure described in detail in Ref. 7. To make use of this code, which is for right-circular cylinders with a uniform data grid that covers the entire surface of the cylinder, zero-valued imperfection data were input for the regions of the LO_2 barrel that were not measured. This step was performed by using a rectangular grid that had 49 points along the barrel length, 521 points along the entire barrel circumference, and a 2×2-in. mesh spacing. Next, a best-fit right-circular cylindrical surface was obtained that corresponds to a least-squares fit of the data. This analysis yielded a best-fit cylinder with a radius $r = 165.385$ in. Then, points of the imperfect-shell surface were defined relative to the best-fit surface. Following this step, the coefficients of a two-dimensional Fourier series representation of the imperfect-shell surface were obtained. The series is given by

$$\bar{w}(x,\theta) = \sum_{k=0}^{23}\sum_{l=0}^{260}\left\{[A_{kl}\cos(l\theta) + B_{kl}\sin(l\theta)]\cos\left(\frac{2k\pi x}{L}\right) + [C_{kl}\cos(l\theta) + D_{kl}\sin(l\theta)]\sin\left(\frac{2k\pi x}{L}\right)\right\} \quad (1)$$

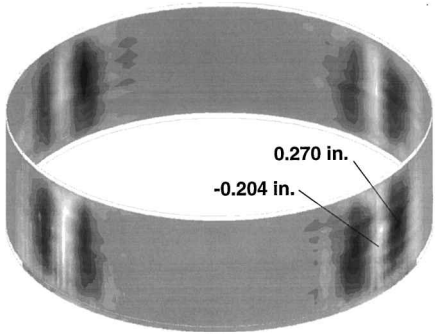

a) Measured imperfection ($A = -0.204$ to 0.270 in.)

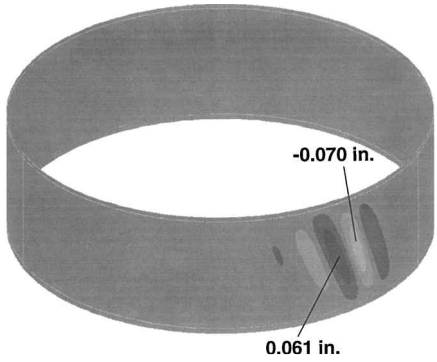

b) Linear bifurcation mode imperfection ($A/t = 0.5$ and $A = -0.070$ to 0.061 in.)

Fig. 4 Measured imperfection and linear-bifurcation buckling mode imperfection shapes (LO_2 barrel section).

where $L = 95.651$ in. and $\bar{w}(x, \theta)$ is the deviation of the imperfect-shell surface that is measured perpendicular to the best-fit surface. A comparison of the surface coordinates of the imperfect-shell surface that were calculated from the Fourier series with the corresponding coordinates of the measured data (referred to the best-fit cylinder) yielded a difference of less than 1.2%.

The initial imperfection shape was implemented into the STAGS analyses by using the user-written subroutine called DIMP.[3] In particular, the Fourier series that was given previously was input directly into DIMP with a series of FORTRAN statements. The resulting shape of the measured imperfection that was generated by STAGS is shown in Fig. 4a. Figure 4a indicates that the maximum outward and inward amplitudes are 0.270 and −0.204 in., respectively. These amplitudes correspond to approximately twice the minimum thickness in the region of the barrel where they are located.

Results and Discussion

The results that are presented herein are closely related to the results that are presented in Refs. 1 and 2 for the prelaunch loading condition with a full LH_2 tank and an empty LO_2 tank. In Refs. 1 and 2, it was shown that the LO_2 tank buckles locally in the barrel section between approximately $\theta = 280$ and 330 deg, as indicated in Figs. 5 and 6. Moreover, results of nonlinear analyses were presented that show a benign effect of initial geometric imperfections in the form of the linear-bifurcation buckling mode with imperfection-amplitude-to-wall-thickness ratios $A/t \leq 1$. More specifically, the imperfection sensitivity study showed that the barrel section exhibits stable postbuckling load-carrying capability that is commonly associated with stable-symmetric bifurcations and weak unstable-asymmetric bifurcations that are associated with shallow, singly curved panels loaded by edge compression and shear loads.

The concern over the welding-induced initial geometric imperfections came later in the development of the SLWT LO_2 tank than the stability issues that are presented in Refs. 1 and 2. At this later stage in the development of the SLWT LO_2 tank, the thickness distribution of the barrel section had matured. This matured thickness distribution differs somewhat from the thickness distribution that was used to generate the results presented in Refs. 1 and 2. Essentially, the matured thickness distribution is thicker in the region

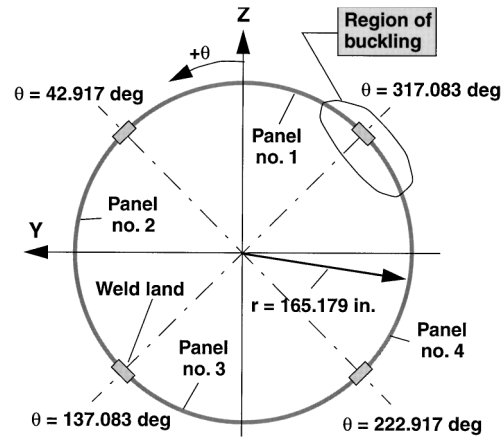

a) Top view

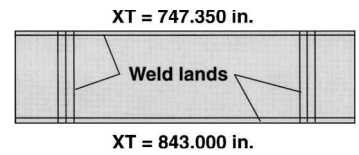

b) Side view

Fig. 5 LO_2 barrel panel layout.

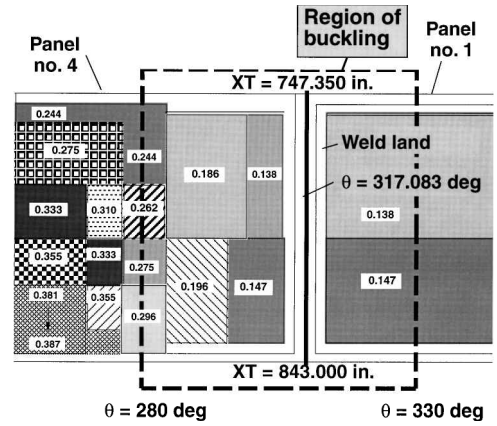

Fig. 6 Thickness distribution of LO_2 barrel in and around the buckle; thicknesses are given in inches.

surrounding the buckle mentioned earlier. (The matured thicknesses in this region are shown in Fig. 6.) This matured thickness distribution was used in the analysis models that were used to obtain all of the results that are presented subsequently.

Three different finite element models were used in the present study to perform a limited convergence study in the analysis of the LO_2 tank that is subjected to the prelaunch loading condition. To identify an adequate model with as few degrees of freedom as possible, linear-bifurcation buckling analyses were conducted first. The passive loads associated with load factor p_b were applied to the STAGS models as a linear prebuckling stress state ($p_b = 1$), and the active (destabilizing) loads associated with load factor p_a were used to obtain the minimum eigenvalue. The models that were investigated had 86,700, 104,600, and 146,700 degrees of freedom. The model that was identified as adequate for predicting the linear-bifurcation buckling behavior is shown in Fig. 7 and corresponds to 146,700 degrees of freedom.

The first linear-bifurcation mode (referred to herein as the linear-bifurcation buckling mode) for the geometrically perfect shell is shown in Fig. 7 for the STAGS model with 146,700 degrees of freedom. The eigenvalue for this model corresponds to active loads that are approximately 4.08 times the magnitude of the corresponding active operational loads shown in Fig. 3. This buckling mode shape is practically identical to the corresponding mode shape shown in Refs. 1 and 2; that is, it is isolated in a portion of the barrel section

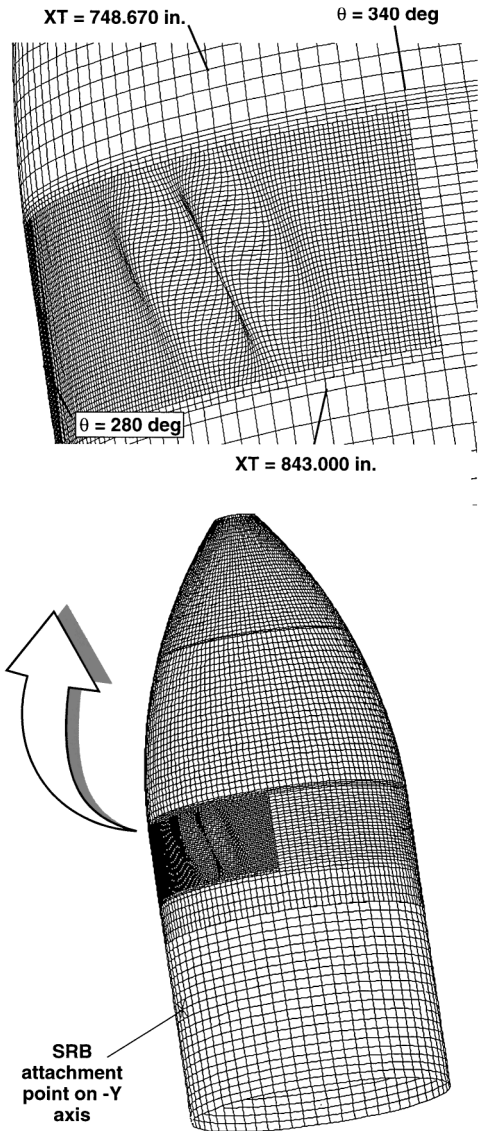

Fig. 7 Linear-bifurcation buckling mode for prelaunch loading condition with full LH_2 tank and empty LO_2 tank; 146,700 degrees of freedom, $p_a = 4.08$ and $p_b = 1.0$.

that envelops the entire length of the barrel and extends from approximately $\theta = 280$ to 330 deg (the quadrant that contains the negative Y-axis and positive Z-axis side of the tank shown in Fig. 5). The large amplitude region for this section is centered approximately on $\theta = 310$ deg. The second through fourth linear-bifurcation modes are also localized, short-wavelength modes, similar to the mode shown in Fig. 7, with eigenvalues equal to 4.21, 4.66, and 4.81, respectively. These eigenvalues are all more than 3% higher than the lowest eigenvalue. The second linear-bifurcation mode is similar to the first mode and is at nearly the same location. The third and fourth modes also have a buckle pattern that is similar in shape to the buckle pattern of the first mode, but the buckled region extends from approximately $\theta = 210$–260 deg (the quadrant that contains the negative Y-axis and negative Z-axis side of the tank shown in Fig. 5).

The isolated nature of the first four linear-bifurcation modes led to the dense mesh refinement of the barrel that is shown in Fig. 7. The mesh refinement was done by increasing the mesh fineness in the local region containing the buckle shown in Fig. 7 and then by eliminating unneeded mesh refinement elsewhere, with care taken not to introduce spurious solutions. This step was facilitated by the use of the five-node and seven-node rectangular transition elements available in STAGS.[3,4] The 104,600- and 146,700-degree-of-freedom models have the same general mesh arrangement shown in Fig. 7, but the level of local refinement of the mesh shown in Fig. 7 for the 146,700-degree-of-freedom model is essentially twice that of the 104,600-degree-of-freedom model. The lowest eigenvalues for the 104,600- and 146,700-degree-of-freedom models are given by $p_a = 4.17$ and 4.08, respectively. The smoothness of the buckling mode shown in Fig. 7 and the approximately 2% difference in the eigenvalues indicate that the 146,700-degree-of-freedom model is adequate for representing the linear-bifurcation behavior of the LO_2 tank for this loading condition. The 104,600- and 146,700-degree-of-freedom models were also used to obtain nonlinear solutions for geometrically perfect and imperfect shells, and in each case the displacement results from the two models differed by 5% or less. These solutions indicate that the 146,700-degree-of-freedom model represents adequately the nonlinear behavior of the LO_2 tank for this loading condition. Thus, all subsequent results presented in this section were obtained with the 146,700-degree-of-freedom model.

Contours of the meridional membrane and shear stress resultants (given in units of pounds per inch) on the negative Y-axis side ($\theta = 270$ deg) of the tank that were obtained from nonlinear analyses are shown in Figs. 8 and 9, respectively, for values of $p_a = p_b = 1$ and for $p_a = 3.91$ and $p_b = 1$. Figures 8 and 9 indicate that high meridional compression stress resultants exist above the thrust panel and that buckling occurs in a region of the barrel where there are significant shear stress resultants. The shear stress resultants are responsible for the slightly skewed appearance of the linear-bifurcation buckling mode shown in Fig. 7.

Results are presented in Figs. 10–12 that show the nonlinear deformations that were obtained from STAGS analyses of a geometrically perfect shell, a geometrically imperfect shell with an imperfection in the form of the linear-bifurcation buckling mode and an imperfection-amplitude-to-wall-thickness ratio $A/t = 0.5$, and a geometrically imperfect shell with the measured imperfection, respectively. The thickness t in the ratio A/t and referred to in Figs. 10–12

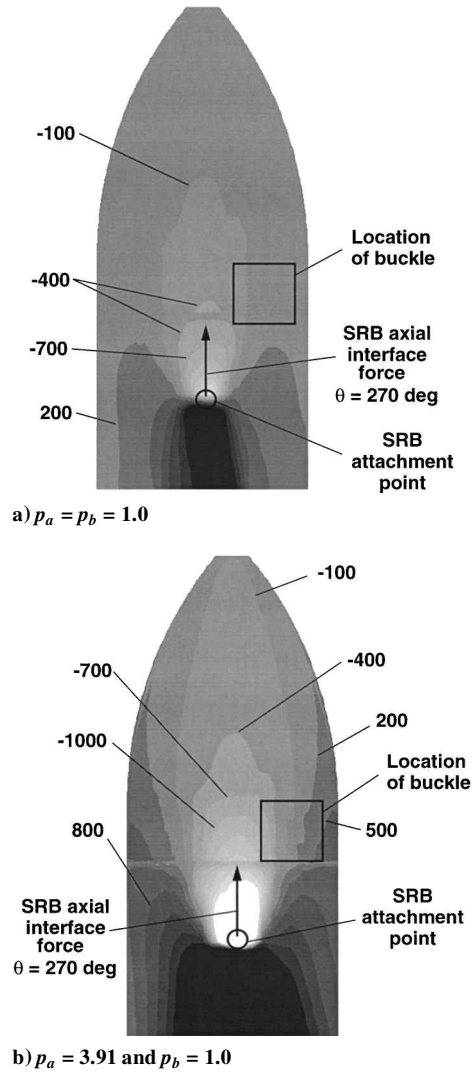

a) $p_a = p_b = 1.0$

b) $p_a = 3.91$ and $p_b = 1.0$

Fig. 8 Meridional membrane stress resultants (pounds per inch).

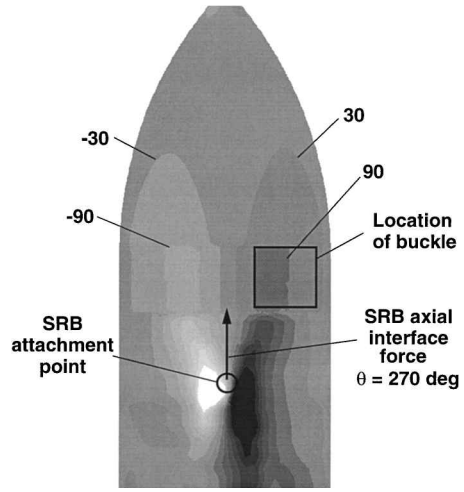

a) $p_a = p_b = 1.0$

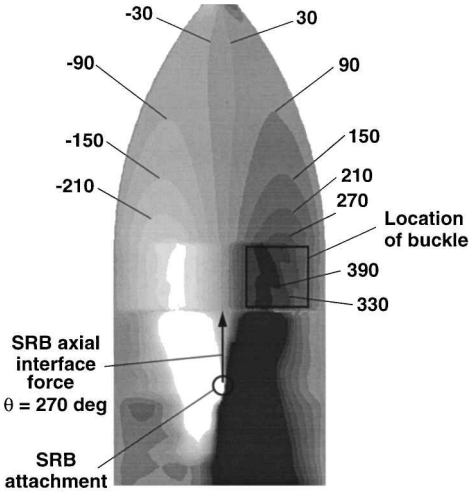

b) $p_a = 3.91$ and $p_b = 1.0$

Fig. 9 Shear stress resultants (pounds per inch).

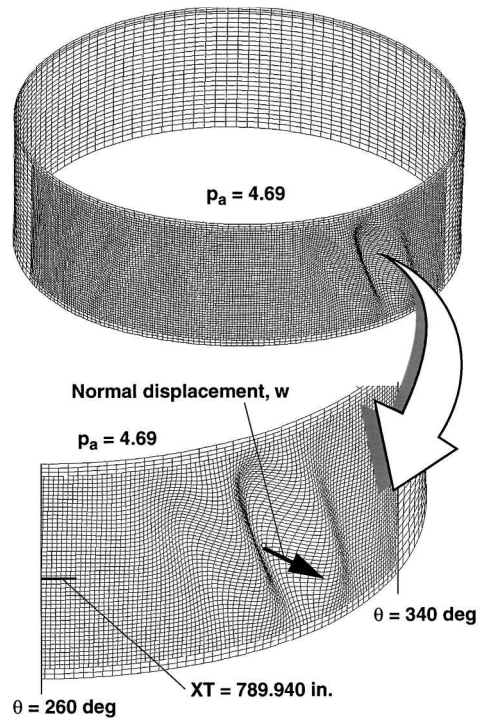

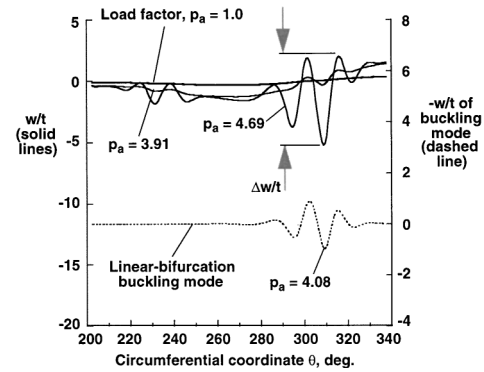

Fig. 10 Nondimensional normal displacement *w/t* of geometrically perfect barrel; *t* = 0.138 in. and *XT* = 789.94 in.

is the minimum wall thickness in the buckled region that is shown in Fig. 6 ($t = 0.138$ in.). For the results shown in Fig. 11, the negative of the linear-bifurcation buckling mode was used as the imperfection shape because it was found to provide a stronger nonlinear interaction with the compressive stresses in the shell wall than the positive-valued imperfection shape. The results shown in Figs. 10–12 are for nonlinear solutions that were obtained by increasing the load factors p_a and p_b simultaneously to a value of one, and then holding p_b constant while increasing the magnitude of the load factor p_a. The nondimensional normal displacements w/t along the circumference of the barrel shell wall at $XT = 789.94$ in. and from $\theta = 200$–340 deg are represented by the solid lines in Figs. 10–12 for values of the load factor p_a approximately equal to 1.0, 3.77–3.91, and 4.43–4.69. The linear-bifurcation buckling mode, the corresponding imperfection shape, and the measured imperfection shape along $XT = 789.94$ in. are given by the dashed lines shown in Figs. 10–12, respectively, with their normalized amplitudes given by the right-hand ordinate of the figures. The linear-bifurcation buckling mode imperfection ($A/t = 0.5$), which is considered to be relatively large for thin shells, is also shown in Fig. 4b and has a much smaller amplitude than the measured imperfection. For this imperfection, the maximum outward and inward amplitudes are 0.061 and −0.070 in., respectively. In addition, the linear-bifurcation buckling mode imperfection is similar in shape to the negative of the measured imperfection. These shapes along $XT = 789.94$ in. are included in Figs. 11 and 12 to give an indication of how the imperfection shape influences the nonlinear solution.

The barrel section that is shown in the top part of Fig. 10 for the geometrically perfect shell indicates a nonlinear deformation pattern that encompasses most of panels number 1 and number 4 and part of panel number 2 (see Fig. 5). The deformation is the most pronounced in the region that extends from approximately $\theta = 280$ to 330 deg and has a pattern that is similar to the linear-bifurcation buckling mode shown in Fig. 7. The solid lines in Fig. 10 indicate that bending deformations begin to grow in the region that encloses the linear-bifurcation buckling mode at approximately $p_a = 3.91$, which is slightly lower in value than the linear-bifurcation buckling load level of $p_a = 4.08$. As the load level is increased to $p_a = 4.69$, the bending deformations in this region become severe and additional bending deformations start to grow in the region that extends from approximately $\theta = 220$ to 250 deg. This growth in the amplitude of the bending deformations corresponds to a reduction in the apparent membrane extensional and shear stiffnesses.

Results that were obtained for the imperfect shells also indicate nonlinear deformation patterns that are similar to the response of the geometrically perfect barrel section that is shown in the top part of Fig. 10. These deformation patterns encompass most of panels number 1 and number 4 and part of panel number 2 (see Fig. 5). Likewise, the deformations are the most pronounced in the region that surrounds the linear-bifurcation buckling mode ($\theta = 280$–330 deg), and these deformations have patterns that are similar to the pattern of the linear-bifurcation buckling mode. Comparison of the solid lines in Figs. 10–12 indicate that bending deformations in the region from

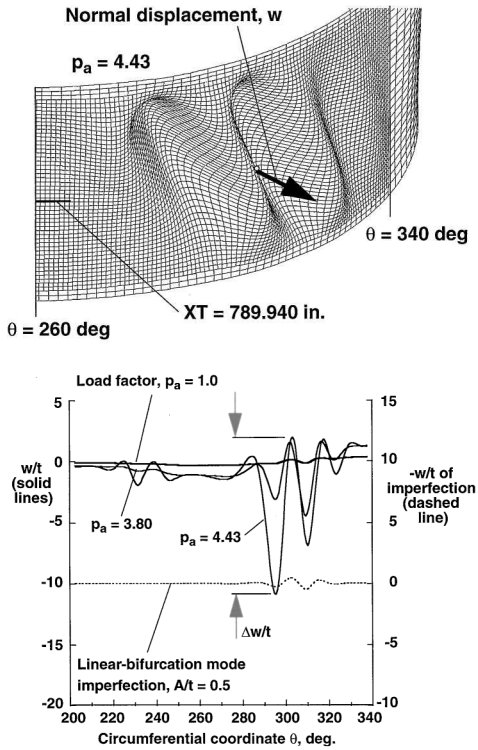

Fig. 11 Nondimensional normal displacement *w/t* of geometrically imperfect shell with linear-bifurcation mode imperfection; *t* = 0.138 in. and *XT* = 789.94 in.

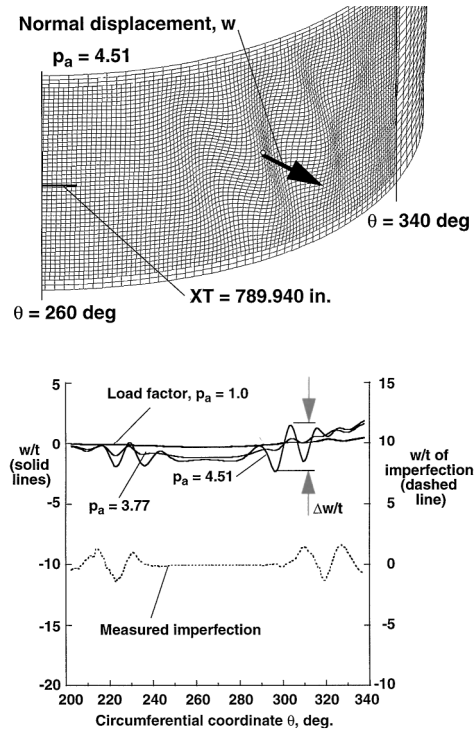

Fig. 12 Nondimensional normal displacement *w/t* of geometrically imperfect shell with measured imperfection; *t* = 0.138 in. and *XT* = 789.94 in.

$\theta = 280$ to 330 deg are significantly more pronounced for the linear-bifurcation buckling mode imperfection, and significantly less pronounced for the measured imperfection, than for the corresponding bending deformations of the perfect shell. This dramatically different behavior of the imperfect shells appears to be a result of the substantial difference in the shape of the two imperfections in the region from $\theta = 290$ to 340 deg.

The results presented in Figs. 10–12 also indicate stable nonlinear responses at load levels greater than the load level predicted by

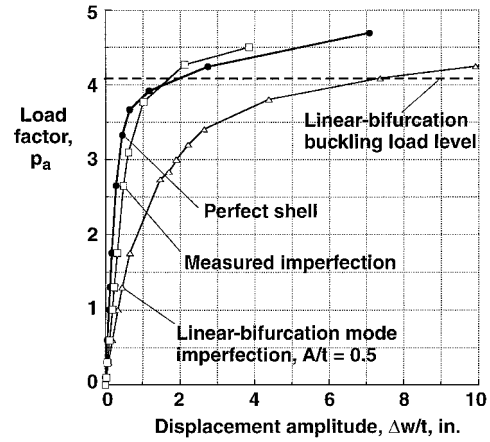

Fig. 13 Local nondimensional normal displacement amplitudes Δ *w/t* of geometrically perfect and imperfect barrels at *XT* = 789.94 in.; *t* = 0.138 in.

the linear-bifurcation buckling analysis ($p_a = 4.08$). At the operational load level given by $p_a = 1$, the results indicate practically no significant nonlinear deformations. As the load level is increased, substantial bending deformations (indicated by the waviness of the curves) develop and grow in the shell wall, and these deformations reduce the apparent membrane extensional and shear stiffnesses of the barrel section. The reduction in the apparent stiffnesses of the barrel is shown more explicitly in Fig. 13 for the geometrically perfect and imperfect shells. In Fig. 13, the intensities of the most severe bending deformations along $XT = 789.940$ in. that are shown in Figs. 10–12 are given as a function of the load factor p_a. The intensity of these severe bending deformations is given by the nondimensional quantity $\Delta w/t$, which is the normalized distance from the maximum value of the local shell-wall displacement to the adjacent minimum value, as shown in Figs. 10–12. The locations of $\Delta w/t$ that are shown in Figs. 10–12 correspond to approximately $\theta = 312$, 299, and 300 deg, respectively. The filled circles shown in Fig. 13 correspond to results for a geometrically perfect shell, and the unfilled triangles and squares correspond to results for the geometrically imperfect shells. In particular, the unfilled triangles and squares correspond to shells with a linear-bifurcation buckling mode imperfection ($A/t = 0.5$) and with the measured imperfection, respectively. The horizontal dashed line shown in Fig. 13 represents the linear-bifurcation buckling load level ($p_a = 4.08$).

The results shown in Fig. 13 indicate that the perfect and imperfect barrel sections of the LO_2 tank exhibit stable postbuckling load-carrying capacity; that is, the geometric imperfections do not cause a premature buckling response. Moreover, the results indicate that the much-smaller-amplitude linear-bifurcation buckling mode imperfection has a more detrimental effect on the nonlinear response than the larger-amplitude measured imperfection. For the geometrically perfect shell and the shell with the measured imperfection, the linear-bifurcation buckling solution gives a reasonable engineering estimate of the onset of a nonlinear shell response that is associated with a large reduction in stiffness for a small increase in load level.

Concluding Remarks

Linear-bifurcation and nonlinear analyses of the Space Shuttle SLWT LO_2 tank have been presented. The loading details for an important prelaunch loading condition have been described and the analytical method used to simulate the loading condition has been discussed. Results have been presented herein that were obtained from complex, large-scale, finite element models of a portion of the Space Shuttle. These results show the effects of actual, measured welding-induced initial geometric imperfections on the nonlinear behavior of the SLWT LO_2 tank for a critical prelaunch loading condition. These results are important because they highlight a commonly encountered type of initial geometric imperfection that was measured for a large-scale launch vehicle. The effect of this type of initial geometric imperfection on the buckling behavior of the SLWT LO_2 tank was previously unknown. Moreover, this type of

initial geometric imperfection may be encountered in the fabrication of other liquid-fuel launch vehicles. In addition, the results indicate that large-scale, high-fidelity, finite element models are generally required to predict accurately the linear-bifurcation and nonlinear responses of these structures.

For the prelaunch loading condition, the analyses predict that the LO_2 tank will buckle in the barrel section, where the actual measured imperfections are located, and will exhibit stable postbuckling behavior at load levels nearly four times the magnitude of the operational load level. The largest degradation in the membrane stiffnesses of the LO_2 tank barrel section is caused by an imperfection shape that is in the form of the linear-bifurcation buckling mode with a relatively small amplitude. The effect of the relatively large-amplitude measured imperfection is benign.

Acknowledgments

The authors would like to express their thanks to V. O. Britt, Walter L. Heard Jr. (retired), Charles C. Rankin, Michael Quiggle, W. Allen Waters Jr., and Neil Otte of Gulf Stream Aerospace, Inc., NASA Langley Research Center, Lockheed Martin Missiles and Space Company, Lockheed Martin Michoud Space Systems Division, Lockheed Martin Engineering Sciences and Services Co., and the NASA Marshall Space Flight Center, respectively, for their technical support.

References

[1] Nemeth, M. P., Britt, V. O., Collins, T. J., and Starnes, J. H., Jr., "Nonlinear Analysis of the Space Shuttle Superlightweight External Fuel Tank," NASA TP-3616, Dec. 1996.

[2] Nemeth, M. P., Britt, V. O., Young, R. D., Collins, T. J., and Starnes, J. H., Jr., "Nonlinear Behavior of Space Shuttle Superlightweight Liquid-Oxygen Tank Under Prelaunch Loads," *Journal of Spacecraft and Rockets*, Vol. 36, No. 6, 1999, pp. 788–803.

[3] Brogan, F. A., Rankin, C. C., and Cabiness, H. D., "STAGS User Manual," Lockheed Martin Missiles and Space Co., Rept. LMSC P032594, Palo Alto, CA, June 1994.

[4] Young, R. D., and Rankin, C. C., "Modeling and Nonlinear Structural Analysis of a Large-Scale Launch Vehicle," *Journal of Spacecraft and Rockets*, Vol. 36, No. 6, 1999, pp. 804–811.

[5] Árbocz, J., and Hol, J. M. A. M., "Shell Stability Analysis in a Computer Aided Engineering (CAE) Environment," *Proceedings of the 34th Structures, Structural Dynamics, and Materials Conference*, AIAA, Washington, DC, 1993, pp. 300–314.

[6] Árbocz, J., and Hol, J. M. A. M., "Koiter's Stability Theory in a Computer-Aided Engineering (CAE) Environment," *International Journal of Solids and Structures*, Vol. 26, No. 9/10, 1990, pp. 945–973.

[7] Árbocz, J., and Williams, J. G., "Imperfection Surveys on a 10-ft-Diameter Shell Structure," *AIAA Journal*, Vol. 15, No. 7, 1977, pp. 949–956.

H. L. McManus
Associate Editor